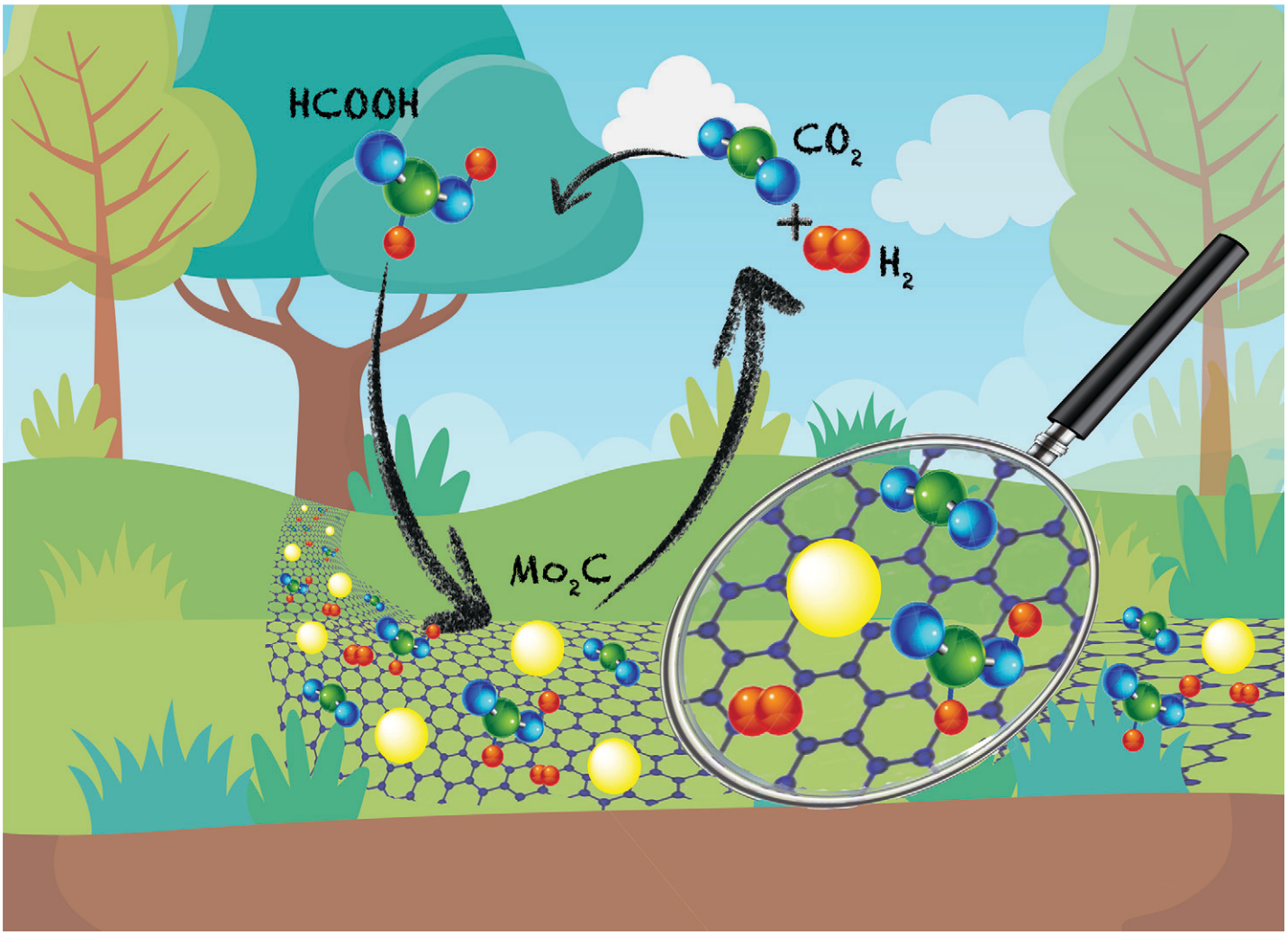

Showcasing research from D.H Carrales-Alvarado, A.B. Dongil, J.M. Fernández-Morales, M. Fernández-García, A. Guerrero-Ruiz and I. Rodríguez-Ramos, Laboratory at Instituto de Catálisis y Petroleoquímica (CSIC) Spain.

Selective hydrogen production from formic acid decomposition over Mo carbides supported on carbon materials

The decomposition of formic acid has received renewed attention due to the possibility of obtaining hydrogen from biomass waste. Molybdenum carbide is a low-cost material that can be well-dispersed on carbon supports. Its synthesis was studied over different carbon materials and results discussed based on structural and spectroscopy characterization. A.B. Dongil acknowledges CSIC for financial support (Project iLink 20211).

As featured in:

See A. B. Dongil, I. Rodríguez-Ramos *et al.*, *Catal. Sci. Technol.*, 2020, **10**, 6790.

ROYAL SOCIETY OF CHEMISTRY

rsc.li/catalysis

Registered charity number: 207890

Catalysis Science & Technology

ROYAL SOCIETY OF CHEMISTRY

PAPER

View Article Online
View Journal | View Issue

Check for updates

Cite this: *Catal. Sci. Technol.*, 2020, 10, 6790

Selective hydrogen production from formic acid decomposition over Mo carbides supported on carbon materials†

D. H. Carrales-Alvarado,[a] A. B. Dongil,*[a] J. M. Fernández-Morales,[b] M. Fernández-García,[ac] A. Guerrero-Ruiz[bc] and I. Rodríguez-Ramos*[ac]

Received 28th May 2020,
Accepted 15th July 2020

DOI: 10.1039/d0cy01088j

rsc.li/catalysis

The decomposition of formic acid to obtain hydrogen has been studied using molybdenum carbides supported on activated carbon and two high surface area graphites, H_{200} (200 m^2 g^{-1}) and H_{400} (400 m^2 g^{-1}). Particular attention is paid to the effect of Mo loading. The catalysts were prepared *in situ* using a mixture of CH_4 and H_2 at a temperature of up to 700 °C. Under these conditions, carburization was mostly complete. We observed that the support influenced the Mo_xC phase obtained so that it seems that the ratio of defective carbon influences the phase. However, for these materials the C/Mo ratio did not influence the obtained crystal phase. Characterization by XRD showed that while the β-Mo_2C phase was obtained over activated carbon and over H_{200}, in contrast, MoO_xC_y was obtained over H_{400}. These catalysts reached 100% conversion on formic acid decomposition at temperatures in the range of 190–250 °C and were also highly selective under these mild conditions, with values for CO_2 selectivity in the range of 85.0–96.5%. The best results were achieved over a 10 wt% Mo loading on activated carbon that reached 96.5% selectivity to H_2. Also, changes in the molybdenum phases were observed on the spent catalyst. Some redox transformations during reaction were responsible for the transformation of β-Mo_2C into oxycarbide MoO_xC_y. In summary, the results of the catalytic performance indicated that the β-Mo_2C phase was more active, selective and stable than MoO_xC_y under the studied conditions.

Open Access Article. Published on 15 July 2020. Downloaded on 12/6/2025 1:38:28 PM.
This article is licensed under a Creative Commons Attribution 3.0 Unported Licence.

1. Introduction

The need to substitute fossil sources with other more environmentally friendly alternatives that match current energy schemes has prompted research on more sustainable energy sources. One of the possibilities is to use hydrogen as an energy vector as it is well known to have a high energy density per mass, and it produces only water upon combustion. However, hydrogen actually holds a low energy per unit volume in the gas phase; thus, it would occupy a large volume which limits its widespread application. Alternatively, hydrogen can be stored in other molecules that are more easily handled and that decompose into hydrogen when required.[1] Among them, formic acid, HCOOH, represents an interesting alternative since it offers a high content of hydrogen (4.3 wt%), it is safe and it is produced in large quantities in biorefineries as a subproduct of the Biofine process.[2] Its attractiveness is also due to the soft conditions required to decompose it into hydrogen and carbon dioxide in the presence of a catalyst. However, under reaction conditions the catalyst may also promote the dehydration reaction of formic acid, producing carbon monoxide and water, which is an undesirable reaction path not only because of the lower hydrogen production but also because carbon monoxide is a poison of catalysts, especially those most commonly employed in fuel cells such as Pt.[3]

Formic acid decomposition over heterogeneous catalysts has been studied over metals in their reduced state,[4] metal oxides and, more recently, immobilized noble metal complexes.[5] Despite the clear potential of these latter systems that could provide a high atom efficiency, their high cost and low stability complicates industrial application.

Moreover, an attractive catalyst should also be easy to synthesize using an environmentally safe process and be cost effective. Some studies using oxides such as α-Fe_2O_3, pure Al_2O_3 and MgO-doped Al_2O_3 appeared; however, their activity and selectivity is low even at temperatures above 200 °C.[6,7]

In this context, the use of transition metal carbides emerges as an interesting alternative since they have proven to be very active and selective in several reactions. The reason

[a] *Instituto de Catálisis y Petroleoquímica, CSIC, c/Marie Curie No. 2, Cantoblanco, 28049 Madrid, Spain. E-mail: a.dongil@csic.es*
[b] *Dpto. Química Inorgánica y Técnica, Facultad de Ciencias UNED, Senda del Rey 9, 28040 Madrid, Spain*
[c] *UA UNED-ICP (CSIC), Grupo de Diseño y Aplicación de Catalizadores Heterogéneos, Madrid, Spain*

† Electronic supplementary information (ESI) available. See DOI: 10.1039/d0cy01088j

This journal is © The Royal Society of Chemistry 2020

Open Access Article. Published on 15 July 2020. Downloaded on 12/6/2025 1:38:28 PM.
This article is licensed under a Creative Commons Attribution 3.0 Unported Licence.

for these results seems to be their structural similarity to Pt group metals. The potential of molybdenum carbide in the production of hydrogen by decomposition of several starting molecules such as methanol or formic acid has already been assessed.[8–10] It was demonstrated that decomposition of formic acid over molybdenum carbide surfaces was enhanced compared to metallic molybdenum even at low temperatures.[9] Indeed, the selectivity obtained over C–Mo (110) was 15 times higher than over Mo (110).

Other authors studied the effect of the carbon source on unsupported molybdenum carbide structure and its relation to formic acid decomposition.[11] One of the challenges of molybdenum carbide to be used in heterogeneous catalysis is obtaining a high surface area material to maximize the activity. In this respect, some alternative synthetic procedures such as those using other carbon precursors have been studied, but still surface areas below 40 $m^2\ g^{-1}$ were obtained.[12] Another possibility is to support the carbide on a high surface area material. In this sense, the use of carbon supports can be beneficial for several reasons. The carbon support may favour the formation of the carbide by providing an additional carbon source for the synthesis. Also, since water might be produced during the reaction, a hydrophobic and stable support under such conditions is preferred.

The effect of the nature of the carbon support and its influence on the catalytic performance on reactions like steam reforming of methanol or dry reforming of methane have been reported.[13]

Still, the catalytic behaviour of carbon-supported molybdenum carbide in formic acid decomposition has been scarcely investigated and assessing the effect of its structure is highly challenging and not fully understood.

Hence, we have studied the synthesis of molybdenum carbide using a mixture of CH_4 and H_2 over two commercial high surface area graphites and we have compared their performance with the activated carbon supported counterpart to evaluate the effect of the graphitic structure.

2. Results

2.1 Characterization

The external surface area of the catalysts was measured for each sample and results are summarized in Table 1. The S_{BET} of the parent supports is 950, 400 and 200 $m^2\ g^{-1}$ for AC, H_{400} and H_{200}, respectively. It can be observed that S_{BET} decreases as the amount of carbide increases. The reduction of S_{BET} for the high surface area graphite-based catalysts is higher than the expected value due to the weight percentage of carbide on the surface. The loss of surface area in carbon supports upon carburization has been well reported and ascribed to pore blocking due to carbon growth during the carburization and/or the metal nanoparticles or to partial gasification of the support.[14] However, considering the structure of high surface area graphites, the observed decrease in surface area is likely due to the agglomeration of the graphite particles upon thermal treatment. The higher loss of surface area on active carbon could be ascribed either to the easier gasification of carbon on that material or particularly to its large number of pores in the microporous range which are easily blocked. The external surface area of the activated carbon without micropores is 400 $m^2\ g^{-1}$.

Diffractograms of molybdenum carbide samples, shown in Fig. 1, differ depending mainly on the type of support.

The XRD patterns of $10Mo_xC/AC$ and $20Mo_xC/H_{200}$ show quite sharp diffractions at 2θ of 34.4°, 37.7°, 39.4° and 61.5°. On the other hand, the catalysts prepared over H_{400}, 5–20 wt% Mo and $10Mo_xC/H_{200}$, display similar XRD profiles showing wide diffractions with maxima shifted to lower angles, *ca.* 2θ of 36.7–36.9°, compared to $20Mo_xC/H_{200}$ and $10Mo_xC/AC$, suggesting the contribution of several phases and/or the amorphous structure of the resulting supported nanoparticles. Moreover, none of the XRD patterns of the fresh catalysts prepared over H_{400} and AC display diffractions of the oxide phases, confirming that the carburization treatment was mostly effective. Nonetheless, the XRD pattern of the catalyst $20Mo_xC/H_{200}$ shows two small diffraction peaks at 2θ of 23.7° and 49.1° corresponding to MoO_3 (JCPDS-PDF 05-0508 and 76-1003).

There are several reports with different assignations for the XRD and no clear consensus exists. In order to assess the carburisation mechanism taking place and the obtained structures, we followed the synthesis of $10Mo_xC/H_{400}$ using *in situ* Mo K-edge X-ray absorption near-edge spectroscopy

Table 1 Textural and physical–chemical properties of the catalysts and intrinsic activity

Catalyst	S_{BET} ($m^2\ g^{-1}$)	d_{TEM} (nm)	Mo/C_{XPS}	Activity (mol CO_2/mol Mo h^{-1})
$5Mo_xC/H_{400}$	217	2.0	0.0049	85
$10Mo_xC/H_{400}$	213	2.2	0.0103	112
$20Mo_xC/H_{400}$	204	3.8	0.0105	73
$10Mo_xC/H_{200}$	107	na	—	61
$20Mo_xC/H_{200}$	72	8.1	—	10
$10Mo_xC/AC$	377	2.1	—	240

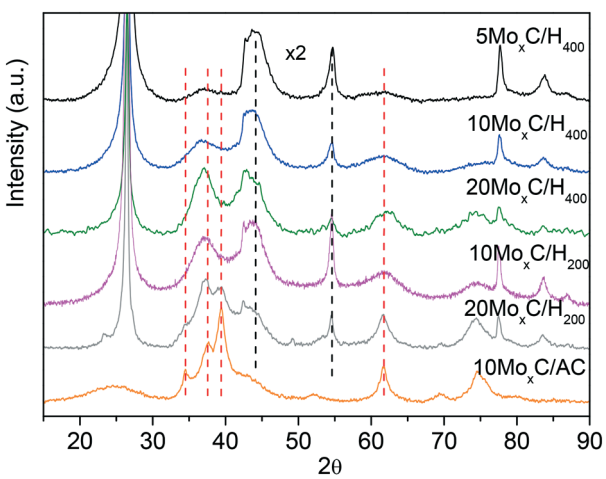

Fig. 1 XRD patterns of the catalysts. Dotted lines represent β-Mo_2C (red) graphite.

Open Access Article. Published on 15 July 2020. Downloaded on 12/6/2025 1:38:28 PM.
This article is licensed under a Creative Commons Attribution 3.0 Unported Licence.

(XANES). The Mo K-edge spectra, shown in Fig. S1,† show the evolution of molybdenum species under a CH_4/H_2/He atmosphere during the temperature treatment. Application of principal component analysis (PCA)[15] to this set of spectra evaluates the number of Mo chemical species involved during the synthesis process and their concentration evolution. This information is summarized in Fig. 2. The absorption edges (obtained using the derivatives of the spectra) were used to estimate the oxidation state of each species by using the linear correlation obtained with the reference Mo compounds (see Fig. S2 and S3†). In Fig. 2B, the two Mo^{6+} species spectra exhibit similar characteristics to those of the AHM reference with a pre-edge feature in the spectra that does not appear in the other Mo species. Thus, the sample initially contains the supported ammonium heptamolybdate (AHM), in which Mo^{6+} is in six-fold coordinated sites (see reference spectra in Fig. S3†). It is possible to observe three characteristic XANES resonances whose relative intensity is influenced by the local order around Mo atoms in octahedral symmetry.[16] Upon heating, the supported AHM is transformed into another Mo^{6+} species also in octahedral coordination, a molybdenum oxide type structure whose XANES spectrum shows a higher intensity of the second XANES resonance relative to the first and third. This indicates changes in the specific surrounding environment of Mo atoms, likely an increase in the cluster size of the molybdenum oxide.[16] This process takes place up to 350 °C when the first Mo^{6+} is mostly absent. Meanwhile, a Mo^{2+} species ascribed to molybdenum oxycarbide,[16] MoO_xC_y, starts to appear at 300 °C while the second Mo^{6+} species decreases. In the temperature range of *ca.* 400–600 °C, the fraction of MoO_xC_y is mostly constant, indicating that simultaneous formation and consumption of MoO_xC_y take place with parallel formation of a Mo^{1+} species with XANES spectrum similar to that corresponding to the molybdenum carbide phase β-Mo_2C (Fig. S2†). Upon heating up to 700 °C, it resulted in further carburisation with a final proportion of *ca.* 90% of β-Mo_2C and 10% of MoO_xC_y.

Based on XANES experiments we can now assign the XRD peaks as follows. The diffraction peaks observed for the catalyst $10Mo_xC/AC$ correspond to the (100), (002), (101) and (110) planes of the β-Mo_2C hcp phase (JCPDS-PDF 77-0720). The higher angle at which the maximum is observed for the other catalysts would be in agreement with the presence of the MoO_xC_y phase that holds a face-centered-cubic (fcc) structure with diffraction peaks at 37.1°, 44.1° and 62.9°.[17,18] It must be noted, however, that XANES showed a higher proportion of β-Mo_2C on the selected $10Mo_xC/H_{400}$ sample than that observed by XRD. This can be attributed to the small size of the supported carbide particles which would be below the detection limit of XRD, *i.e.* <5 nm, as the TEM images in Fig. 3 and S4† also confirmed. In contrast, for $10Mo_xC/AC$, both large and small particles are carburised as the XRD and HRTEM images showed. For this sample, well-resolved lattice fringes of 0.23 nm that correspond to the β-Mo_2C (101) planes are observed in particles as small as 2 nm. Similar findings are observed for $10Mo_xC/H_{400}$, for which β-Mo_2C (101) is also observed in small particles.

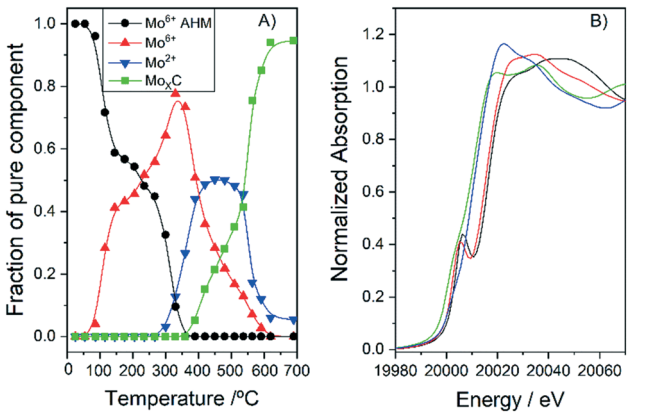

Fig. 2 Concentration profiles (A) and Mo K-edge XANES spectra (B) of the different pure Mo species observed during the synthesis of $10Mo_xC/H_{400}$.

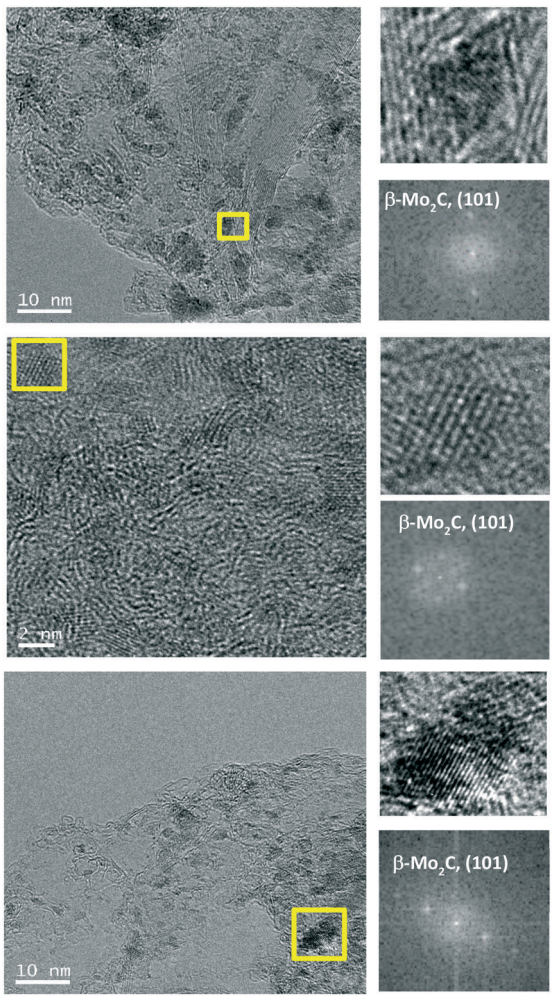

Fig. 3 Typical HRTEM images of $10Mo_xC/H_{400}$ (top); $10Mo_xC/AC$ (middle) and $20Mo_xC/H_{200}$ (bottom) and the corresponding fast-Fourier transform (FFT) pattern.

This journal is © The Royal Society of Chemistry 2020

Open Access Article. Published on 15 July 2020. Downloaded on 12/6/2025 1:38:28 PM.
This article is licensed under a Creative Commons Attribution 3.0 Unported Licence.

Hence, it can as well be inferred that larger particles are more difficult to carburise. This is in agreement with the diffraction peaks ascribed to MoO_3 observed on $20Mo_xC/H_{200}$ which is the sample with the largest particle size, *ca.* 8.1 nm, as estimated by TEM and shown in Table 1.

The XRD patterns of the samples with different Mo loading also seem to indicate that under the studied conditions the Mo/C loading did not influence the obtained carbide phase.

It has been reported that the synthesis of molybdenum carbides through the TPR method may follow one of these paths: (a) first, the decomposition of the molybdate precursor into MoO_3 takes place, which is then reduced to MoO_2 to finally result in β-Mo_2C. (b) Alternatively, after MoO_3 formation, this oxide may undergo partial carburization to an oxycarbide MoO_xC_y, which is eventually transformed into β-Mo_2C.[19] This latter path, proposed in the literature, agrees quite well with the XANES results obtained in the present work, where both oxycarbide and β phases are observed.

With the aim of gaining more information on the synthesis mechanism and the effect of the support, additional XANES experiments were performed with the $20Mo_xC/H_{400}$ sample but in a H_2/He atmosphere. The analysis of the *in situ* Mo K-edge XANES spectra (Fig. S5†) showed that the same MoO_3, MoO_xC_y and β-Mo_2C species are obtained as when CH_4/H_2/He is employed over the $10Mo_xC/H_{400}$ sample (see Fig. 2 and 4). These results suggest that under the studied conditions, the carbon source that afforded the carbide is the support itself independently of the reaction atmosphere. Similar results were reported previously for temperatures below 600 °C.[19] The slight differences between samples, *i.e.* the $20Mo_xC/H_{400}$ is somewhat more resistant to reduction, in agreement with XRD experiments, may be attributed to effects of the different particle sizes in the samples (Table 1). The $20Mo_xC/H_{400}$ sample with larger particles is more difficult to carburize.

Also, considering these stages, it is reasonable to presume that the availability of more reactive carbon atoms from the support would aid in the formation of β-Mo_2C. In this sense, the carbon supports are characterized by their different proportions of edges to basal planes, *i.e.* the size of the graphitic layers, so that a higher proportion of edges means more reactive carbon. This feature is given by the Raman spectra that allow comparison by using the intensity of the so-called D and G bands.[20] The Raman spectra of the supports (in Fig. S6)† used in the present work show that the I_D/I_G ratio follows the trend AC > H_{400} > H_{200}. Since external CH_4 does not seem to be involved in the carburisation mechanism, we performed H_2-TPR experiments coupled to mass spectrometry on the impregnated samples $10Mo_xC/H_{200}$, $10Mo_xC/H_{400}$ and $10Mo_xC$/AC to assess for differences among the supports. The masses corresponding to the main fragments of H_2O (*m*/*z* 18), CO (*m*/*z* 28), CO_2 (*m*/*z* 44) and

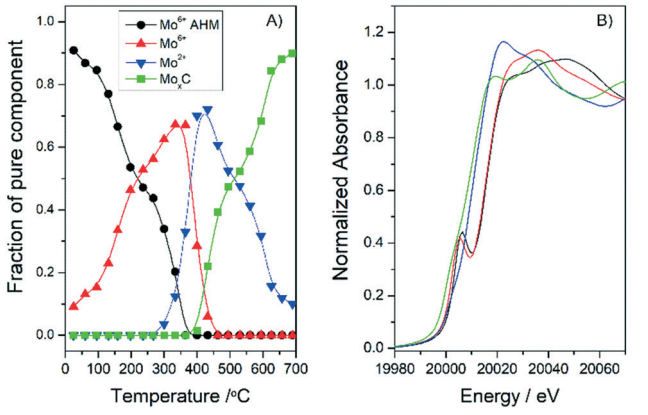

Fig. 4 Concentration profiles (A) and Mo K-edge XANES spectra (B) of the different pure Mo species observed during the treatment of Mo_{20}/H_{400} in a H_2/He atmosphere.

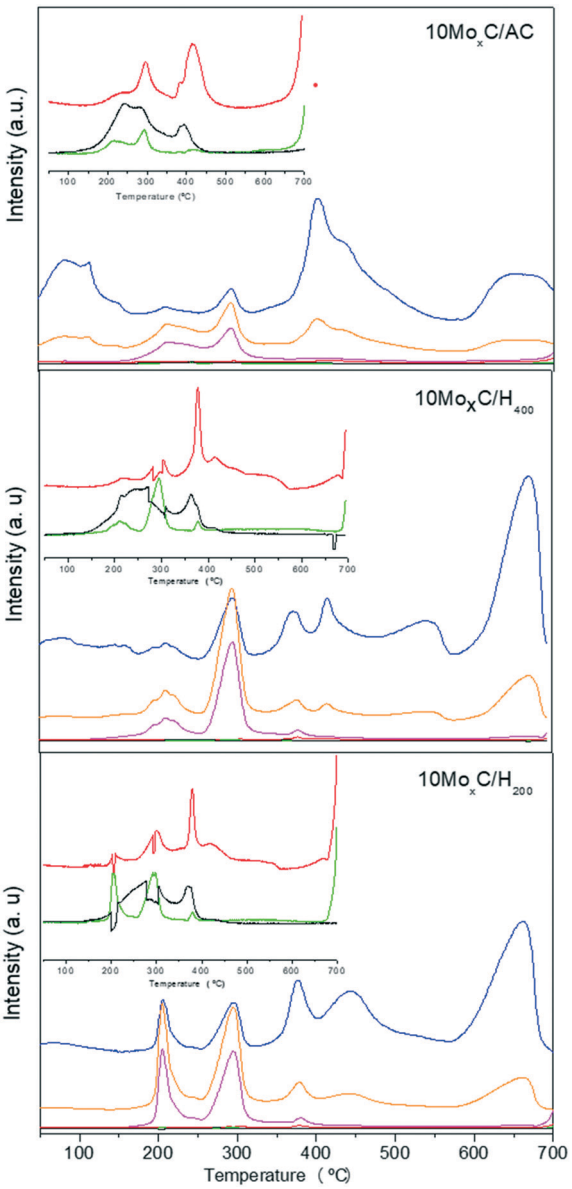

Fig. 5 MS profiles during H_2-TPR of impregnated samples. *m*/*z*: (—) 14, (—) 16, (—) 17, (—) 18, (—) 28, (—) 44.

Open Access Article. Published on 15 July 2020. Downloaded on 12/6/2025 1:38:28 PM.
This article is licensed under a Creative Commons Attribution 3.0 Unported Licence.

NH_3 (*m*/*z* 17) and the secondary fragments of CH_4 (*m*/*z* 14) were followed along with other secondary fragments of H_2O and NH_3 (*m*/*z* 16, 15) and are shown in Fig. 5.

The three samples displayed the evolution of *m*/*z* 18–16 and 17 with the maxima at 200–210 °C and 290 °C in a proportion that indicates they correspond to NH_3 and H_2O. These gases would be generated from the decomposition of the precursor, AHM, and the temperature range agrees with that observed in XANES for this transformation.

At higher temperatures, the profile is different for $10Mo_x$-C/AC. This sample shows a maximum at 400 °C in which contributions of *m*/*z* 18–16 are observed in a proportion that suggests that they correspond to H_2O. The same masses are observed at *ca.* 600 °C but the intensity of these latter peaks is lower. Small intense signals for *m*/*z* 28 and 44 at *ca.* 290 °C and 415 °C are also observed. The samples $10Mo_xC/H_{200}$ and $10Mo_xC/H_{400}$ also display contributions of *m*/*z* 18–16 which can be ascribed to H_2O. However, the maxima appeared at 400 °C and 660 °C, the latter being the most intense peak. Also, simultaneous evolution of *m*/*z* 28 due to CO is also observed, although its intensity is very low.

The XANES results suggested that the source of carbon is the support itself and that carburisation already starts at 300 °C, with the formation of the oxycarbide which is then transformed into β-Mo_2C as shown in the following reaction.

$$MoO_3 + C^* + H_2 \rightarrow MoO_xC_y + H_2O \rightarrow \beta\text{-}Mo_2C + CO$$

In this range of temperatures, carburisation must be preceded by the formation of gaseous carbon species, most likely CH_4 coming from the reaction with hydrogen and releasing H_2O. However, the intensity of *m*/*z* 16–14 in the profiles up to 700 °C does not suggest the evolution of CH_4, and only above that temperature, an intense peak started to appear. We believe this is due to the consumption of the evolved CH_4 in the carburisation process.

Also, the different intensities of the MS-TPD peaks at 400 °C and 600 °C for AC and the two H samples seem to indicate that the extent to which the first step occurs on AC is greater than on H_{200} and H_{400} samples. This is reasonable since in this first step the incorporation of carbon takes place and, as already pointed out, activated carbon holds a larger proportion of reactive carbon atoms. In turn, it also suggests that carburisation took place to a larger extent, as XRD also showed.

Regarding previous literature results, it has been reported that the synthesis of molybdenum carbide over carbon nanofibers and carbon nanotubes using the TPR method (CH_4/H_2) also led to the formation of β-Mo_2C and that above 700 °C no molybdenum oxide was observed.[21,22] Other authors also analysed the effect of the surface chemistry and structural properties of the support using an oxidized graphite and oxidized activated carbon.[23] Although a clear correlation of surface chemistry and structural properties with the formed molybdenum phase was difficult to obtain, the authors suggested that the defective carbon was somehow responsible for the formation of β-Mo_2C and that the controlled reduction of the molybdenum precursor was a critical factor to determine the formed crystal phase.

Some authors proposed that the Mo/C ratio on an ordered mesoporous carbon support controls the Mo_xC phase.[24] We observed that samples with different loading, mainly $10Mo_xC/H_{200}$ and $20Mo_xC/H_{200}$, displayed different XRD profiles. However, this seems to be more related to the contribution of larger particles to the XRD profile, which are present in a higher ratio on samples with greater loading.

Our results are in agreement with some literature reports that indicated oxycarbide and β-Mo_2C as the only detected phases. We can add that even in a CH_4/H_2 atmosphere the source of carbon is the support itself. Also, the fact that the support is the source of carbon is in agreement with the easy carburisation of smaller particles that would be in closer contact with the support.

2.2 Reaction results

The conversion of formic acid decomposition measured at each temperature is given in Fig. 6A for all the tested catalysts. As the figure shows, all the catalysts were active; however the temperature at which 100% conversion was reached varied greatly in the range 190 °C to 250 °C. Among the catalysts, the conversion curve was very similar for the samples $10Mo_xC/H_{400}$, $20Mo_xC/H_{400}$ and $10Mo_xC$/AC, while

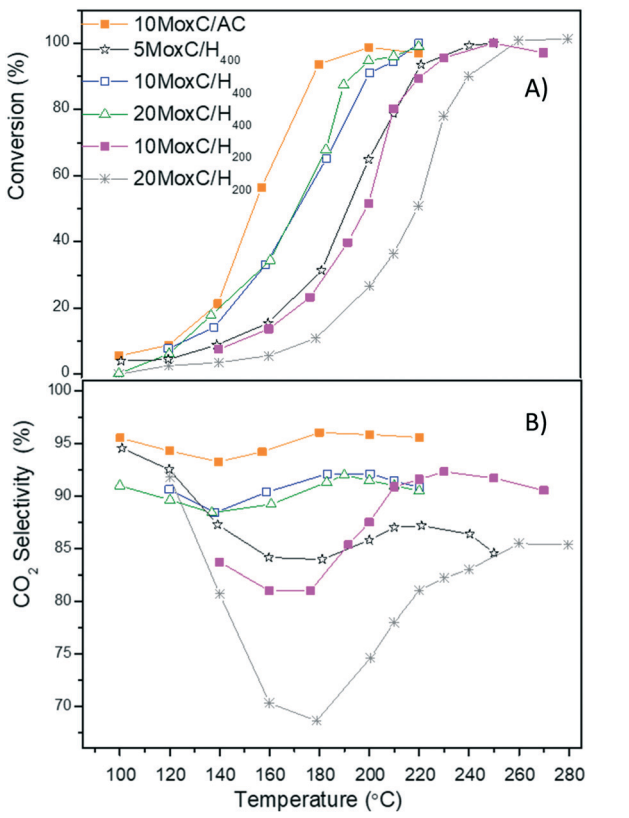

Fig. 6 (A) Conversion of FA *vs.* *T* and (B) CO_2 selectivity *vs.* *T*. Reaction conditions: 1 bar, GHSV = 20 000 h^{-1}.

This journal is © The Royal Society of Chemistry 2020

Open Access Article. Published on 15 July 2020. Downloaded on 12/6/2025 1:38:28 PM.
This article is licensed under a Creative Commons Attribution 3.0 Unported Licence.

those of $5Mo_xC/H_{400}$, $10Mo_xC/H_{200}$ and $20Mo_xC/H_{200}$ shifted to higher temperatures.

In order to minimize the effect of Mo loading, the activities at 150 °C were estimated and the results are displayed in Table 1.

The activity follows the trend $10Mo_xC/AC > 10Mo_xC/H_{400} > 5Mo_xC/H_{400} > 20Mo_xC/H_{400} > 10Mo_xC/H_{200} > 20Mo_xC/H_{200}$. The activity values and the similar particle size of the carbide on $10Mo_xC/H_{400}$ and $10Mo_xC/AC$ seem to indicate that the catalyst presenting exclusively the β-Mo_2C phase is more active than those in which MoO_xC_y appeared as well. Regarding the effect of metal carbide loading, the activities for the sample with 10 wt% Mo supported on H_{400} was significantly higher than those of 5 wt% and 20 wt%. According to the microscopy results, carbide nanoparticles are larger on the sample with higher loading, $20Mo_xC/H_{400}$, in agreement with the similar Mo/C surface ratio obtained by XPS for $10Mo_xC/H_{400}$ and $20Mo_xC/H_{400}$, shown in Table 1. This can explain straightforwardly the lower activity of $20Mo_xC/H_{400}$ and suggests that in the studied system, above 10% wt Mo there is an optimum loading before particles tend to form large agglomerates that diminish the active area, as observed in other carbon-supported systems.[25] A similar and even more clear effect is observed for the catalysts supported on H_{200}.

The selectivity to CO_2 at each temperature (Fig. 6B) was estimated considering the total concentration of CO_2 and CO as the only detected products and revealed significant differences. The catalysts displayed maximum selectivity in the range 85.0–96.5%, with the catalyst $10Mo_xC/AC$ offering the best selectivity among the tested systems. This also points to a beneficial effect of the β-Mo_2C phase compared to MoO_xC_y.

Indeed, if we compare the selectivity achieved with the catalysts $10Mo_xC/AC$ and $10Mo_xC/H_{400}$, it is clear that the different phases influence the concentration of H_2 in the products. While with $10Mo_xC/AC$ selectivity to CO_2 reached 96.5% at conversions above 50%, with $10Mo_xC/H_{400}$ the selectivity for conversions over 50% was 91%.

Regarding molybdenum-based catalysts, previous literature reported that 100% formic acid conversion was achieved at temperatures above 250 °C for unsupported molybdenum carbide systems[11] and over 200 °C for supported systems over activated carbon with selectivity of around 98%.[26] However, the catalysts employed in ref. 11 and 26 were prepared using a liquid phase mixture with organic compounds that is less attractive from an industrial point of view and may leave impurities on the catalysts.

Nevertheless, the reported catalytic performance using molybdenum carbide and our own results are better than those reported for non-noble metal systems like metal oxides such as α-Fe_2O_3 for which maximum conversion was around 24% at a temperature of 200 °C with low selectivity to H_2 (ref. 7 and 27) and other systems where Ag and Mg were used as dopants for Mo_xC that reached 90% selectivity.[28]

Interestingly, the selectivity profiles with temperature shown in Fig. 6B are similar. All the catalysts prepared over high surface area graphite showed an initial selectivity decrease up to 140–180 °C, which corresponds to formic acid conversions in the range of 10–12% followed by a selectivity increase, at temperatures up to above 200–260 °C, *i.e.* when conversion reached 90%. These results are in agreement with previously reported selectivity profiles where other authors observed that CO_2 selectivity decreased with temperature in the temperature range 100–150 °C.[6] However, the evaluation of the catalysts at higher temperatures performed in the present work shows that selectivity increased from conversions above 15%, and at 95% conversion the selectivity decreased again.

As long as the stability is concerned, additional experiments in time on stream at temperatures of 180–190 °C for all the catalysts and at 220 °C for $20Mo_xC/H_{200}$ were performed for 12 hours. Both conversion and selectivity profiles (Fig. 7) remain stable with time for all the catalysts, except for the conversion achieved with $20Mo_xC/H_{200}$ that showed a continuous decrease with time, while selectivity was constant.

It is known that the decomposition of formic acid may take place through two paths: dehydrogenation ($HCOOH \rightarrow H_2 + CO_2$) and dehydration ($HCOOH \rightarrow CO + H_2O$). Also, the water gas shift and/or the reverse reaction may take place producing $CO_2 + H_2$ or CO and H_2O, respectively.[1]

According to DFT studies described in the literature, the surface of molybdenum carbide leads exclusively to the formation of CO_2 and H_2 since both Mo and C sites can

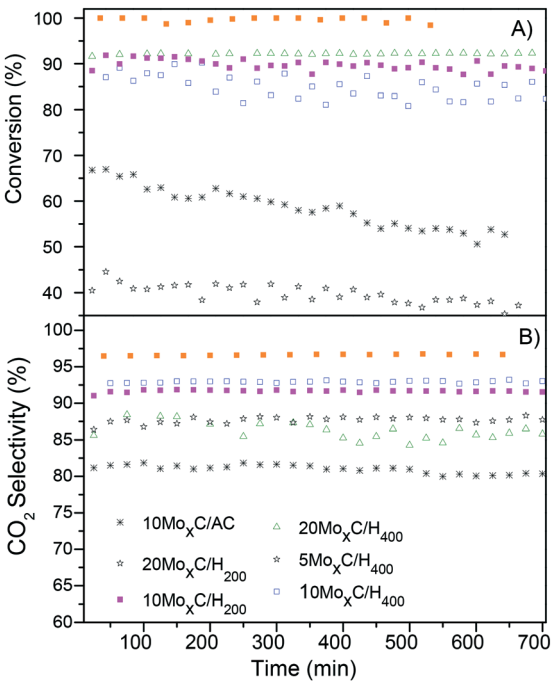

Fig. 7 Time-on-stream (A) conversion of FA and (B) CO_2 selectivity; reaction conditions: 1 bar, *T*: 180–190 °C (220 °C for $20Mo_xC/H_{200}$), GHSV = 20 000 h^{-1}.

Open Access Article. Published on 15 July 2020. Downloaded on 12/6/2025 1:38:28 PM.
This article is licensed under a Creative Commons Attribution 3.0 Unported Licence.

chemisorb oxygen and eliminate it as CO_2.[8] Also, the simulations performed in that investigation suggested that molybdenum carbide decreased the rate of dehydration (undesired reaction to form CO + H_2O).

Regarding the WGS reaction, theoretical studies reported that neither Mo^0 nor Mo-terminated Mo_2C is active in the WGS reaction.[29] However, oxygen-covered C-terminated surfaces, O–C–Mo_2C, were active in WGS apparently due to the formation of oxycarbide species as a consequence of the presence of H_2O. Moreover, we performed additional reaction tests using molybdenum oxide supported on H_{400} and tested in the FA decomposition. The results indicated that molybdenum oxide is active above 190 °C when conversion reached 16%, but selectivity to CO_2 was 22% (see Fig. S7†).

Thus, considering the potential reactions and the selectivity profiles, we could explain the results as follows. β-Mo_2C would be selective to the dehydrogenation of FA, producing mainly CO_2 + H_2. The presence of small amounts of a different phase other than β-Mo_2C produced during the reaction on 10Mo_xC/AC, *i.e.* MoO_xC_y and/or molybdenum oxide, could explain the 96.5% selectivity to CO_2 obtained with that catalyst.

On the other hand, for the catalysts presenting also MoO_xC_y, it is plausible that both FA dehydrogenation and dehydration occur at the beginning of the experiment and when conversion reaches 10% the CO and H_2O formed through dehydration react to produce CO_2 and H_2 *via* the water gas shift reaction, thus increasing the selectivity. If this happens it is plausible that only limited oxidation of molybdenum carbide occurs since water would be consumed by the WGS reaction. Hence, we performed XRD on the spent catalysts to assess for potential changes and are shown in Fig. 8 labelled as "catalyst-PR".

However, different results were observed. On the one hand, 10Mo_xC/H_{400}-PR displayed diffractions at 2θ of 34.4°, 37.7°, 39.6° and 61.5° and sharper than those of the fresh catalyst that correspond to sintered particles of the β-Mo_2C phase. On the other hand, 20Mo_xC/H_{400}-PR shows diffractions at 2θ of 35.2° and 36.7° and at 2θ of 53.5°, which can be ascribed to MoO_2.[30,31] For 5Mo_xC/H_{400}-PR, no diffractions other than those of the support were observed. This is probably due to the small particle size and/or the low concentration of species below the detection limit.

In any case, the detected changes on the catalysts phase, either conversion to β-Mo_2C or to oxycarbide, agree with the selectivity profiles observed for 10Mo_xC/H_{400}-PR and 20Mo_xC/H_{400}-PR since both new phases may promote the CO_2 selectivity either by direct transformation of FA to CO_2 or through the WGS reaction.

A different case is that of the catalyst 20Mo_xC/H_{200}. This catalyst initially presented both carbide and oxide phases and the selectivity to CO_2 is below that of the other tested catalysts, but it also showed a selectivity increase at around 10% conversion. The XRD pattern of the spent catalyst shows diffractions at 2θ of 34.4°, 37.8°, and 39.8° from β-Mo_2C along with peaks at 35.7°, 38.2° and 60.1°. The position of these latter peaks seems to indicate that they correspond to oxycarbide. Again, it seems that oxycarbide is formed during the reaction, and although the β-Mo_2C phase is still detected, the intense and sharp diffraction ascribed to oxycarbide seems to indicate that large particles of this species have been formed on the surface. Despite the appearance of these new nanoparticles, the selectivity remained stable with time probably due to the positive effect of the new oxycarbide species which are active in the WGS reaction. However, the larger particle size inferred from the sharp XRD peaks would be responsible for the conversion decrease with time.

In contrast, the XRD pattern of the 10Mo_xC/AC sample after reaction also corresponds to β-Mo_2C and no other diffraction is envisaged, in agreement with the higher selectivity to CO_2 and better stability. Nonetheless, the selectivity below 100% could also suggest that small undetected amounts of another phase are present. Thus, even in the presence of oxidants, H_2O or CO_2, this catalyst was highly stable under the reaction conditions.

The changes of the molybdenum phase under the reaction conditions have already been reported. For example, during dry reforming of methane, deactivation of β-Mo_2C catalysts due to oxidation to MoO_2 has been reported.[32] Ledoux *et al.* also found that β-Mo_2C changed to MoO_2, while α-Mo_xC was transformed into MoO_2 and eventually to β-Mo_2C.[19] Similarly, phase changes were also observed in the spent catalysts after steam reforming of methanol.[33]

Some authors have reported that other phases such as α-MoC are more active on formic acid decomposition than β-Mo_2C.[5] However, chloro- and nitrogen-containing compounds were used as the carbon source to prepare the catalysts and the effect of those elements should have been considered. Indeed, in the same report it is also shown that a conventional β-Mo_2C prepared from a CH_4/H_2 mixture was the most active and selective catalyst. In line with our results, molybdenum carbide prepared over activated carbon was more active and selective than when carbon nanotubes were used as support.[6] Even though the crystallographic phase of

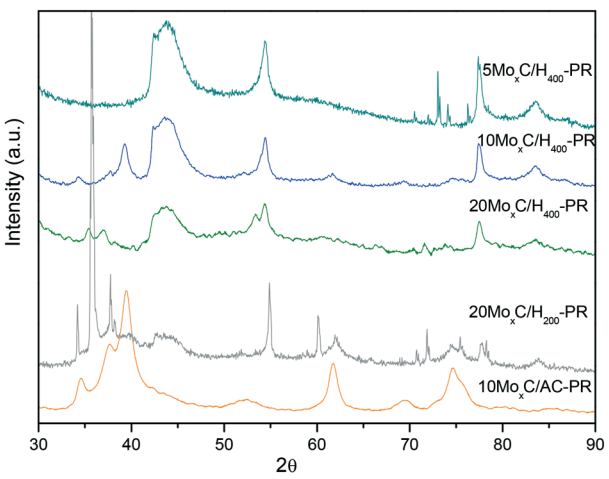

Fig. 8 XRD patterns of the spent catalysts.

This journal is © The Royal Society of Chemistry 2020

Open Access Article. Published on 15 July 2020. Downloaded on 12/6/2025 1:38:28 PM.
This article is licensed under a Creative Commons Attribution 3.0 Unported Licence.

the molybdenum carbides was not shown, it is likely that the β-Mo_2C phase was formed over activated carbon as already shown in several literature reports and in the present work.[23,26] As demonstrated by XRD, in the present work the main phase on the catalysts was β-Mo_2C, although MoO_xC_y could be found on H_{400} and H_{200} based catalysts, so our results are in quite good agreement with the literature, showing that β-Mo_2C is more active and selective.

Very recently, the reaction mechanisms of both dehydration and dehydrogenation reactions of formic acid on molybdenum carbide have been studied.[34] The authors proposed that the target reaction leading to CO_2 and H_2 takes place through bridged formate species that evolve into monodentate formate and transformed to CO_2 and H* following a Langmuir–Hinshelwood mechanism. On the other hand, the dehydration reaction follows an Eley–Rideal path in which gaseous HCOOH reacts with adsorbed H* to form H_2O and CO. Considering these paths, the rate in which dehydrogenation occurs might depend on the ease of the bridge-type adsorption of the formate.

The carbon/molybdenum ratio influences the physicochemical properties of the carbides and thus the catalytic properties. In this sense, it has already been reported that a higher C/Mo ratio has a negative impact on the reactivity. In this respect, the MoO_xC_y surface would be more saturated and less metallic than the unsaturated Mo_2C surface.[35] Following this argument, it is plausible that the cleavage of the O–H bond and adsorption of the formate on the less saturated surface of β-Mo_2C would be energetically favoured compared to that over MoO_xC_y.

3. Experimental

3.1 Synthesis of materials

Metal carbides were prepared by wetness impregnation followed by carburization treatment. Activated carbon (Type CO-850 from Petrochil S.A.) was used as support and was first ground and sieved to <150 μm particle size and then dried at 110 °C for 2 h before impregnation. Commercial high surface area graphite (H_{400} and H_{200}) was obtained from Timcal Graphite.

An aqueous solution of the precursor $(NH_4)6Mo_7O_{24}$ (99% from Aldrich) was impregnated on the support using the corresponding amount to obtain the metal loading, left for maturation for 6 h, and dried overnight at 80 °C. The carburization was carried out *in situ* prior to the reaction, under an 80/20 mixture of H_2/CH_4 (% vol) at 700 °C (5 °C min^{-1}) for 2 h. The resulting catalysts were labelled according to the metal composition, loading and support.

3.2 Characterization

The textural properties were measured from the adsorption isotherm of N_2 at −196 °C using a 3Flex instrument from Micromeritics. Around 100 mg were previously degassed for 4 h at 110 °C under vacuum using a SmartVacPrep instrument from Micromeritics. The surface area was calculated from the adsorption branch in the range $0.02 \leq p/p_0 \leq 0.25$ using the Brunauer–Emmett–Teller (BET) theory. Total pore volume was defined as the single-point pore volume at $p/p_0 = 0.99$.

X-ray diffraction (XRD) patterns of the passivated catalysts were acquired in the 2θ range between 4° and 90° with a step of 0.04° s^{-1} using a Polycrystal X'Pert Pro PANalytical diffractometer with Ni-filtered Cu Kα radiation (λ = 1.54 Å) operating at 45 kV and 40 mA.

XPS measurements were performed with an energy analyser (PHOIBOS 150 9MCD, SPECS GmbH) using non-monochromatic Al radiation (200 W, 1486.61 eV). The samples were pelletized and transferred to the outgassed chamber. Prior to the experiments, the samples were outgassed *in situ* for 24 h to achieve a dynamic vacuum below 10^{-10} mbar. The binding energy (BE) was measured by reference to the C 1s peak at 284.6 eV, with an equipment error of less than 0.01 eV in the energy determinations.

Information about the supported metal particles was acquired by TEM in a JEOL 2100F field emission gun electron microscope operated at 200 kV and equipped with an energy-dispersive X-ray detector. The sample was ground into powder and a small amount was suspended in ethanol solution using an ultrasonic bath. Some drops were added to the copper grid (Aname, Lacey carbon 200 mesh) and the ethanol was evaporated at room temperature before introducing it into the microscope. Scanning transmission electron microscopy (STEM) was done using a spot size of 1 nm. The average particle size area (d_{TEM}) was calculated as

$$d_{TEM} = \frac{\sum n_i d_i^3}{\sum n_i d_i^2}$$

Mo K-edge (20 000 eV) X-ray absorption near-edge spectra (XANES) were recorded in dispersive mode at the BM23 beamline at the European Synchrotron Radiation Facility (ESRF, Grenoble, France). The catalysts were pressed into pellets and sieved to a size between 0.090 and 0.140 mm. The samples (*ca.* 15 mg) were loaded in a quartz plug-flow microreactor system developed at BM23. The reactor was continuously fed with (a) 30 mL min^{-1} of a 20/5/75 mixture composition of H_2/CH_4/He for the temperature-programmed carburization experiment or (b) 30 mL min^{-1} of 20% hydrogen in helium during the temperature-programmed reduction experiment. The temperature was raised by 3 °C min^{-1} up to 700 °C. XANES spectra were collected every 30 °C or 10 min during the heating.

3.3 Reaction

The measurements of the catalyst activity in vapor phase formic acid decomposition were carried out in a fixed-bed flow reactor. The catalysts (0.075 g) were placed in a U-tube reactor with an internal diameter of 4 mm. All the samples were *in situ* carburized in CH_4/H_2 (20 : 80 vol) at 700 °C for 2 h and cooled in N_2 to the reaction temperature prior to testing (*in situ* reduction). A mixture of 5.5 vol% formic acid/

Open Access Article. Published on 15 July 2020. Downloaded on 12/6/2025 1:38:28 PM.
This article is licensed under a Creative Commons Attribution 3.0 Unported Licence.

N_2 at a total flow rate of 25 cm^3 (STP) min^{-1} was fed to the reactor by a saturator. The reactants and products were analysed using a gas chromatograph (Varian 3400) fitted with a 60/80 Carboxen TM 1000 column and a thermal conductivity detector. At each temperature, a few measurements were performed to ensure that steady-state activity was reached. During the test, the unique products determined were CO, CO_2 and H_2. The concentrations of these compounds were calculated by the following equations.

$$[H_2] = \frac{\text{Area } H_2}{RF} \qquad [CO_2] = \frac{\text{Area } CO_2}{RF} \qquad [CO] = \frac{\text{Area CO}}{RF}$$

As the formation of products different from those indicated was negligible, the total conversion of formic acid was determined as the sum of CO and CO_2 concentrations related to the initial concentration of formic acid.

$[HCOOH]_0 = [CO]_m + [CO_2]_m$ at T_{max} to obtain a complete conversion of HCOOH

To determine the conversion of formic acid, it was necessary to calculate the concentration of CO and CO_2 using the following equation.

$$X_{HCOOH} = \frac{[CO] + [CO_2]}{[HCOOH]_0} \times 100$$

In addition, the selectivity to CO_2 was calculated. The catalysts were studied in two heating cycles. The stability of the catalyst was evaluated over 18 hours at a selected temperature. Tests with the bare supports proved that conversion was negligible.

Conclusions

The synthesis of molybdenum carbide by the TPR method using a CH_4/H_2 feed was performed successfully over activated carbon and two high surface area graphites, H_{200} and H_{400}, of different graphitic layer dimensions. The formed carbide nanoparticles were between 2.0 and 8.1 nm in size, which depended on the surface area and metal loading. Also, characterization showed that the carbide phase was influenced by the support. Accordingly, when activated carbon was used, the β-Mo_2C phase was obtained almost exclusively. However, over H_{400} and H_{200}, the oxycarbide phase MoO_xC_y was also observed. We explained the differences based on the graphitic layer size. This is related to the availability of defective carbon which in turn favours the carburisation. Interestingly, XANES experiments showed that even under a CH_4/H_2 atmosphere the main source of carbon is the support itself. This also implies that smaller particles, which are in closer contact with the support, are more easily carburised.

The different molybdenum carbide phases influence the catalytic performance. The results showed that the β-Mo_2C phase is more active and selective than MoO_xC_y. However, since MoO_xC_y is also active in the WGS reaction, the selectivity to CO_2 increases during the reaction. Moreover, β-Mo_2C supported on activated carbon proved to be stable under the reaction conditions.

Conflicts of interest

There are no conflicts to declare.

Acknowledgements

We acknowledge financial support from the Spanish Agencia Estatal de Investigación (AEI) y el Fondo Europeo de Desarrollo Regional (FEDER), UE (projects CTQ2017-89443-C3-1-R and CTQ2017-89443-C3-3-R). The ESRF synchrotron is thanked for granting beamtime at BM23. A. B. Dongil acknowledges financial support from the Fundación General CSIC (Programa ComFuturo). DHCA thanks the Consejo Nacional de Ciencia y Tecnologia, CONACyT, Mexico for a postdoctoral fellowship [grant numbers 2018-000022-01EXTV-00519, 2019-000029-01EXTV-00057. We acknowledge support of the publication fee by the CSIC Open Access Publication Support Initiative through its Unit of Information Resources for Research (URICI).

Notes and references

1 B. Dou, H. Zhang, Y. Song, L. Zhao, B. Jiang, M. He, C. Ruan, H. Chen and Y. Xu, *Sustainable Energy Fuels*, 2019, **3**, 314.

2 (*a*) D. J. Hayes, S. Fitzpatrick, M. H. B. Hayes and J. R. H. Ross, *The Biofine Process – Production of Levulinic Acid, Furfural, and Formic Acid from Lignocellulosic Feedstocks in Biorefineries—Industrial Processes and Products: Status Quo and Future Directions*, ed. B. Kamm, P. R. Gruber and M. Kamm, Wiley-VCH, Weinheim, 2006, pp. 139–164; (*b*) A. Kumar Singh, S. Singh and A. Kumar, *Catal. Sci. Technol.*, 2016, **6**, 12–40.

3 (*a*) J. Wang, J. Zheng, J. Cao, X. Hao, Z. Wang, A. Abudula and G. Guan, *Energy Convers. Manage.*, 2018, **164**, 122; (*b*) J. Wang, J. Cao, Y. Ma, X. Li, P. Xiaokaiti, X. Hao, T. Yu, A. Abudula and G. Guan, *Energy Convers. Manage.*, 2017, **147**, 166.

4 (*a*) G. H. Gunasekar, H. Kim and S. Yoon, *Sustainable Energy Fuels*, 2019, **3**, 1042; (*b*) W. Gan, P. J. Dyson and G. Laurenczy, *ChemCatChem*, 2013, **5**, 3124; (*c*) W. Gan, P. J. Dyson and G. Laurenczy, *React. Kinet. Catal. Lett.*, 2009, **98**, 205; (*d*) Y. Zhao, L. Deng, S.-Y. Tang, D.-M. Lai, B. Liao, Y. Fu and Q.-X. Guo, *Energy Fuels*, 2011, **25**, 3693.

5 G. H. Gunasekar, H. Kim and S. Yoon, *Sustainable Energy Fuels*, 2019, **3**, 1042–1047.

6 I. E. Wachs and D. E. Fein, *J. Catal.*, 2002, **210**, 241–254.

7 S. A. Halawy, S. S. Al-Shihry and M. A. Mohamed, *Catal. Lett.*, 1997, **48**, 247–251.

8 (*a*) Á. Koós and F. Solymosi, *Catal. Lett.*, 2010, **138**, 23–27; (*b*) Q. Luo, T. Wang, G. Walther, M. Beller and H. Jiao, *J. Power Sources*, 2014, **246**, 548–555.

9 Y. Ma, G. Guan, X. Hao, J. Cao and A. Abudula, *Renewable Sustainable Energy Rev.*, 2017, **75**, 1101–1129.

 This journal is © The Royal Society of Chemistry 2020

Open Access Article. Published on 15 July 2020. Downloaded on 12/6/2025 1:38:28 PM.
This article is licensed under a Creative Commons Attribution 3.0 Unported Licence.

10 D. W. Flaherty, S. P. Berglund and C. B. Mullins, *J. Catal.*, 2010, **269**, 33–43.
11 J. Cao, J. Wang, Y. Ma, X. Li, P. Xiaokaiti, X. Hao, A. Abudula and G. Guan, *J. Alloys Compd.*, 2018, **735**, 1463–1471.
12 J. Q. Chi, K. L. Yan, W. K. Gao, B. Dong, X. Shang, Y. R. Liu, X. Li, Y. M. Chai and C. G. Liu, *J. Alloys Compd.*, 2017, **714**, 26–34.
13 (*a*) P. Liang, H. Gao, Z. Yao, R. Jia, Y. Shi, Y. Sun, Q. Fan and H. Wang, *Catal. Sci. Technol.*, 2017, **7**, 3312–3324; (*b*) H. Gao, Z. Yao, Y. Shi and S. Wang, *Catal. Sci. Technol.*, 2018, **8**, 697–701.
14 H. Wang, S. Liu and K. J. Smith, *Energy Fuels*, 2016, **30**, 6039–6049.
15 (*a*) C. Máırquez-Alvarez, I. Rodríguez-Ramos, A. Guerrero-Ruiz, G. L. Haller and M. J. Fernáındez-García, *J. Am. Chem. Soc.*, 1997, **19**, 2905–2914; (*b*) F. R. García-García, M. Fernández-García, M. A. Newton, I. Rodríguez-Ramos and A. Guerrero-Ruiz, *ChemCatChem*, 2013, **5**, 2446–2452.
16 A. Tougerti, E. Berrier, A.-S. Mamede, C. La Fontaine, V. Briois, Y. Joly, E. Payen, J.-F. Paul and S. Cristol, *Angew. Chem., Int. Ed.*, 2013, **52**, 6440–6444.
17 S. T. Oyama, P. Delporte, C. Pham-Huu and M. J. Ledoux, *Chem. Lett.*, 1997, 949–950.
18 A. Hanif, T. Xiao, A. P. E. York, J. Sloan and M. L. H. Green, *Chem. Mater.*, 2002, **14**, 1009–1015.
19 C. Bouchy, C. Pham-huu and M. J. Ledoux, *J. Mol. Catal. A: Chem.*, 2000, **162**, 317–334.
20 A. B. Dongil, L. Pastor-Pérez, A. Sepúlveda-Escribano and P. Reyes, *Appl. Catal., A*, 2015, **505**, 98–104.
21 L. Souza Macedo, R. R. Oliveira, T. van Haasterecht, V. Teixeira da Silva and H. Bitter, *Appl. Catal., B*, 2019, **241**, 81.
22 E. F. Mai, M. A. Machado, T. E. Davies, J. A. Lopez-Sanchez and V. T. da Silva, *Green Chem.*, 2014, **16**, 4092–4097.
23 B. Frank, Z. L. Xie, K. F. Ortega, M. Scherzer, R. Schlögl and A. Trunschke, *Catal. Sci. Technol.*, 2016, **6**, 3468–3475.
24 J. Han, J. Duan, P. Chen, H. Lou, X. Zheng and H. Hong, *ChemSusChem*, 2012, **5**, 727–733.
25 A. B. Dongil, L. Pastor-Pérez, N. Escalona and A. Sepúlveda-Escribano, *Carbon*, 2016, **101**, 296–304.
26 Y. Tao, L. Tao, Z. Pan, S. Qiu and X. Shen, *Fuel*, 2018, **217**, 106–110.
27 D. E. J. Fein and I. E. Wachs, *J. Catal.*, 2002, **210**, 241–254.
28 J. Wang, J. Cao, Y. Ma, X. Li, P. Xiaokaiti, X. Hao and G. Guan, *Energy Convers. Manage.*, 2017, **147**, 166–173.
29 P. Liu and J. A. Rodriguez, *J. Phys. Chem. B*, 2006, **110**, 19418–19425.
30 P. Delporte, C. Pham-Huu, P. Vennegues, M. J. Ledoux and J. Guille, *Catal. Today*, 1995, **23**, 251–267.
31 M. Tsuji, T. Miyao and S. Naito, *Catal. Lett.*, 2000, **69**, 195–198.
32 J. B. Claridge, A. P. E. York, A. J. Brungs, C. Marquez-Alvarez, J. Sloan, S. C. Tsang and M. L. H. Green, *J. Catal.*, 1998, **180**, 85–100.
33 B. Frank, K. Friedel, F. Girgsdies, X. Huang, R. Schlögl and A. Trunschke, *ChemCatChem*, 2013, **5**, 2296–2305.
34 J. T. Gray, S. W. Kang, J. I. Yang, N. Kruse, J. S. McEwen, J. C. Park and S. Ha, *Appl. Catal., B*, 2020, **264**, 118478.
35 T. Wang, X. Tian, Y. Yang, Y. W. Li, J. Wang, M. Beller and H. Jiao, *Phys. Chem. Chem. Phys.*, 2015, **17**, 1907–1917.